 CMES, vol.38, no.2, pp.149-178, 2008

A meshfree poly-cell Galerkin (MPG) approach for problems of elasticity and fracture

C. Zheng[1], S. C. Wu[2,3,4] X. H. Tang[1] and J. H. Zhang[1]

Abstract: A novel meshfree poly-cell Galerkin method is developed for problems of elasticity and fracture. To improve accuracy, a poly-cell support is proposed to ensure the alignment of shape function support and the integration domain. By orthonormalizing basis functions, the improved moving least-square is formulated soundly, in which frequent matrix inversions are avoided. The Nitsche's method is introduced to treat the essential boundary conditions. It is found that computed solutions are more accurate than those obtained using the circle support used in standard MLS. Furthermore, numerical results present the superconvergent property, compared with the theoretical values in both displacement and energy norms. In fracture analyses, the stress intensity factors can be evaluated independent of J-integral path with better accuracy, and rather smooth stress field can be achieved, even near to region of the crack tip. It is also found the present MPG works well even for extremely distorted meshes.

Keywords: Meshfree; Poly-cell local support; Improved MLS; Superconvergence; Fracture.

1 Introduction

The finite element method (FEM) [Zienkiewicz and Taylor (2000)] has been widely applied to solve various type problems of engineering and science in the past several decades. However, due to its strong reliance on the element mesh, there are some inherent shortcomings in simulating such as problems of highly nonlinear, large deformation and crack propagations with arbitrary paths [Belytschko, Lu and Gu (1995)]. To tackle these problems, meshfree methods have been alternatively

[1] College of Water Resources and Hydropower, Sichuan University, Chengdu, 610065 P. R. China
[2] School of Material Science and Engineering, Hefei University of Technology, Hefei, 230009, P. R. China
[3] Centre for Advanced Computations in Engineering Science (ACES), Department of Mechanical Engineering, National University of Singapore, 9 Engineering Drive 1, 117576 Singapore
[4] Corresponding author. Email: wushengchuan@gmail.com

developed and significant progress has been achieved in recent years. They include the element-free Galerkin method (EFG) [Belytschko, Lu and Gu (1994)], the reproducing kernel particle method (RKPM) [Liu, Jun and Zhang (1995)], the meshless local Petrov-Galerkin method (MLPG) [Atluri and Zhu (1998), Atluri, Sladek, etc (2000)] and the point interpolation method (PIM) [Liu (2002), Wu, Liu, Zhang and Zhang (2008), Cui, Liu, Li, Zhao, Nguyen and Sun (2008)], *etc*. As a novel numerical technique typically independent of element meshes, meshfree methods have also been used to solve fracture problems [Atluri and Shen (2002), Sukumar, Moran and Belytschko (1998), Gu and Zhang (2008), Ching and Batra (2001), Fleming, Chu, Moran, Belytschko (1997), Brighenti (2005)].

The background mesh is employed in conducting the EFG regardless of the actual geometrics and a regular mesh is preferred generally. Compared with FEM, meshfree methods based on the background mesh have more difficulty in accurate integration. This is mainly due to the boundary misalignment of integration domains and shape function supports [Liu, Zhang, Wang, Zhong, Li, Han (2006)].

The stabilized nodal integration method is then presented, but the nodal volume is not easy to evaluate [Bessel and Belytschko (1994)], especially for 3D problems of complex geometries. To evaluate the volume of nodal support [Zhou, Wen, Zhang, Zhang (2003)], The Voronoi diagrams are thereafter adopted, and other meshfree methods based on the Voronoi diagrams are formulated [Atluri and Zhu (1998), Braum and Sambridge (1995), Zheng, Zhang and Wu (2008)]. However, the generation of Voronoi diagram is actually very time-consuming and more expensive than the Delaunay triangulation used in the standard FEM [Idelsohn, Onate, Calvo, Facundo (2003), Idelsohn and Onate (2006)].

S.N. Atluri developed a type of true meshfree method [Atluri, S.N. and Zhu, T.L. (1998); Atluri S.N. and Shen S.P. (2002)], which has been widely used in the problems of large deformation, metal forming, multi-scale, dynamic fracture, moving boundary and phase change and etc. [Atluri, S.N (2004); Atluri, S. N., Han, Z. D. and Rajendran, A. M. (2004); Atluri, S.N., Liu, H.T. and Han, Z.D. (2006); Atluri, S.N., Liu, H.T and Han, Z.D. (2006); Han. Z. D. and Atluri, S. N. (2004); Han Z. D., Rajendran, A. M and Atluri, S. N. (2005); Han ZD, Liu HT, Rajendran AM, et al. (2006), Sladek J., Sladek V., Atluri, et al. (2004); Sladek J., Sladek V. , et al. (2005)] In MLPG, local-Galerkin weak form in order to avoid the need for a background mesh and integrations are performed on subdomains surrounding the nodes[Atluri, S.N. and Shen, S. (2005)].

The present work introduces a novel Galerkin meshfree approach. In order to improve the accuracy of numerical integration in Galerkin methods, a poly-cell local support is introduced. This local support can make sure of the alignment of integration domains and shape functions supports, which will be detailed in Sec. 2.

Moreover, in the standard moving least square (MLS) interpolation [Lu, Belytschko and Gu (1994)], orthonormalized basis functions are used and a novel scheme of obtaining the orthonormalized basis functions is presented. This type of MLS is termed as the improved MLS, which avoids the frequent matrix inversion. This good property permits one to construct interpolation functions with general nodes even when the number of nodes is small or irregularly distributed.

For most of meshfree methods, the treatment of essential boundary conditions is not as simple and trivial as the standard FEM, due to the absence of Kronecker delta property of shape functions. The Lagrange multiplier method [Sonia and Antonio (2004)] can impose the essential boundary conditions weakly, but it increases the total number of unknowns and the resulted global stiffness is no longer positive definite. Though the penalty method is widely used without increasing the dimensions of discretized system equations, it is very probable to result in the ill-conditioned system of equations owing to the too large scale parameter. In the present work, the Nitsche's method [Sonia and Antonio (2004)] is introduced to treat the essential boundary conditions. It has a scale parameter as well, but not very large values are required for the implementation. More important is that the global stiffness obtained is symmetric and positive definite. This implies that the system equations can be solved efficiently and performed using the well-developed code for FEM with very little modification.

This paper is outlined as follows. Sec. 2 briefs the construction of poly-cell local support domain. In Sec. 3, the improved MLS approximation is formulated in details based on the classical MLS scheme. Sec. 4 presents the procedure of Nitsche's method for the enforcement of essential boundary conditions, and then derives the discretized system equations for elasticity problems. Sec. 5 conducts an intensive study of elasticity and cracks to demonstrate the properties of the present MPG. Finally, some conclusions are drawn in last Sec. 6.

2 2. Poly-cell support construction

In the construction of mesh-free trial function, each node possesses a domain that is usually termed as "domain of influence" or "local support". Generally, this type of local support is a circular domain or rectangular domain centered by an interested node [Atluri and Zhu (1998), Belytschko, Lu and Gu (1995)]. Furthermore, this trial function support is *not* identical with the integration domain, which results in extra computational difficulty and especially inaccurate domain integration. To better discretize the problem domain and improve the numerical accuracy, a novel poly-cell local support is proposed to replace the traditional local support.

In the poly-cell local domain, a background mesh is firstly generated that may cover

the whole problem domain. The background mesh can be either Voronoi diagram [Zheng, Zhang and Wu (2008)] or regular mesh, and the regular rectangular mesh shown in Fig. 1a is preferred in this paper. For an arbitrary node, its host cell needs to be found firstly, and then the local support domain can be obtained by extending the size of host cell in four directions (x_+, x_-, y_+, y_-). The nodal support domain so constructed is named the poly-cell local support of given node. The extending distance in direction x_+ can be sampled as

$$d_{eI}^{x_+} = n_e c_x \tag{1}$$

where c_x is the size of host cell in the x direction, n_e is a constant integer (n_e=2 in this work). The extending distances in other directions are obtained in the similar way.

After obtaining the local support, the weight function requires to be defined based on this poly-cell local domain. Suppose a node$I$ has a local support shown in Fig. 1b, then the weight function of node I is defined by

$$w_I(x,y) = [f(x)g(y)]^{\alpha} \tag{2}$$

$$f(x) = \begin{cases} \frac{(x-x_I^{\min})(x-x_I^{\max})}{(x_I-x_I^{\min})(x_I-x_I^{\max})} & \text{if } x_I^{\min} < x < x_I^{\max} \\ 0 & \text{else} \end{cases} \tag{3}$$

$$g(y) = \begin{cases} \frac{(y-y_I^{\min})(y-y_I^{\max})}{(y_I-y_I^{\min})(y_I-y_I^{\max})} & \text{if } y_I^{\min} < y < y_I^{\max} \\ 0 & \text{else} \end{cases} \tag{4}$$

where α is a constant parameters larger than 1.0, which will be studied in Sec. 5.

Compared with the traditional circular and rectangular local support, the poly-cell local support domain has at least two advantages:

(i) It guarantees the alignment of integration domain and support of the shape functions, which can significantly improve the accuracy of numerical integration. Moreover, all the points in a certain integration domain possess the same set of supporting nodes. If a "cell" is defined as an integration sub-domain, and an "element" is defined as an area possessing the same set of supporting nodes, then in MPG, each cell also possesses an "element". This good property makes the code for MPG have the very similar form as that of standard FEM.

(ii) The evaluation of distance between integration point and field node is avoided, and the computation order is always of order N^2(N is the number of total field nodes). Instead, neighboring cells always need to be found, which is also required in FEM to allocate the general stiffness matrix (If the band property is

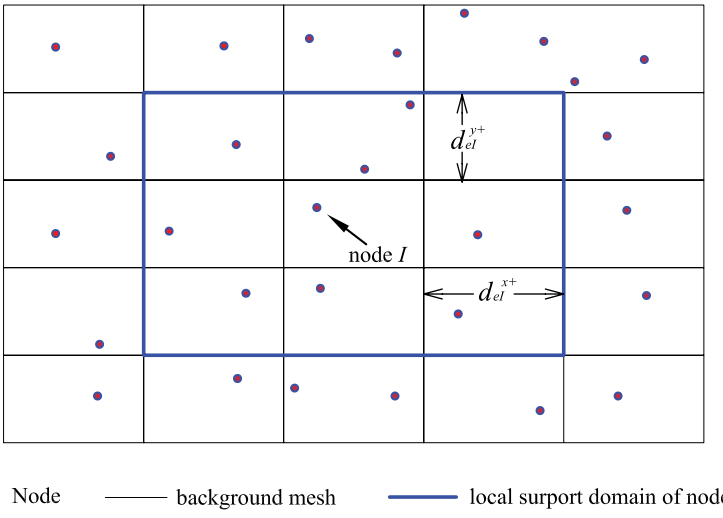

(a) Schematic of constructing poly-cell local support based on regular background mesh.

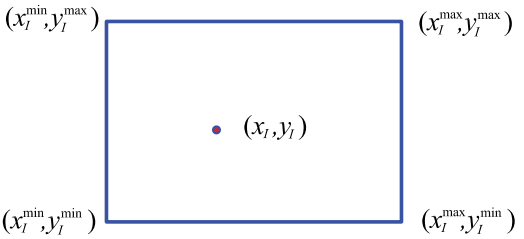

(b) A sampling local support of interested node I. Note that this node may not be at the center of the support domain.

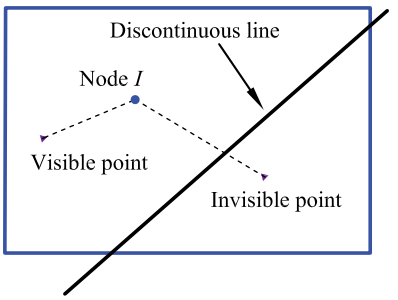

(c) Illustration of the poly-cell support with intersecting the discontinuous line.

Figure 1: Poly-cell local support construction based on regular background rectangular mesh.

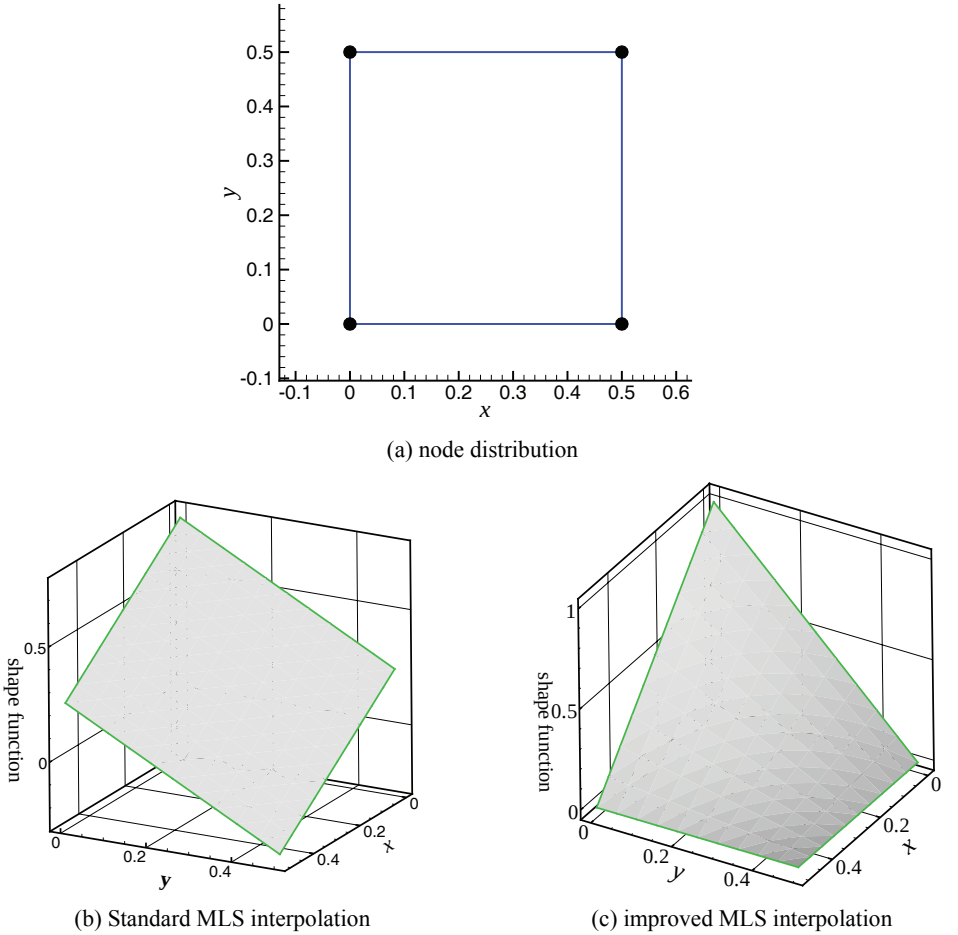

(a) node distribution

(b) Standard MLS interpolation

(c) improved MLS interpolation

Figure 2: A comparison of standard MLS and improved MLS interpolation

used to reduce the cost of memory). Thus the time cost in the computation will be of order N after a simple program organization.

In fracture problems, there exists displacement discontinuity when the poly-cell intersects a progressive crack. The way of dealing with discontinuity in MPG is similar to other meshfree methods, and the "visible criteria" is utilized in the present paper. As clearly illustrated in Fig. 1c, the existence of discontinuous line makes some integral point invisible, at which the weight value of the interested node I is 0.0 when constructing the trial function and nonzero at those of visible point.

In addition, to improve the accuracy, many times of local refinement are usually

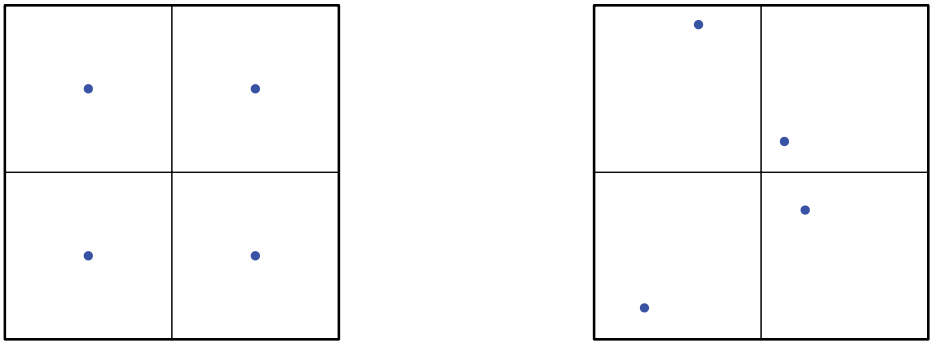

(a) 4 regular nodes (b) 4 irregular nodes

Figure 3: Nodes distributions for the standard patch test, 2×2 model of mesh is adopted

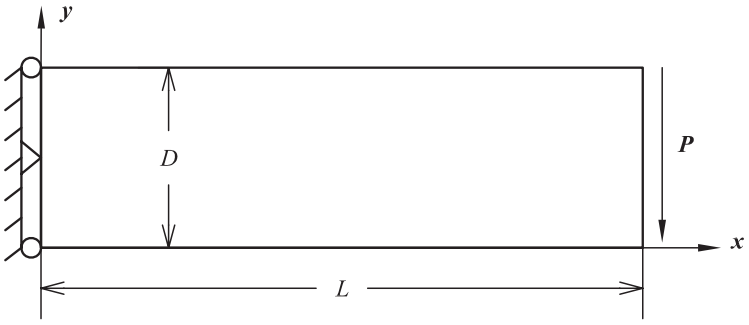

Figure 4: A 2D cantilever beam subjected to parabolic traction on the right end

required especially close to the crack tip. This definitely results in too many support nodes of an interested Gaussian point, which also needs too much time for the construction of trial functions. In the present implementation, for the cells in the mesh degeneration zone, their neighboring cells are divided into four parts by four directions (x_+, x_-, y_+, y_-). The minimum size of the neighboring cells and host cell is used as the extending distance c_x in each part. This modification can sharply reduce the time cost for constructing shape functions in fracture problems.

3 Improved moving least-square method

The MLS approximate scheme is now a commonly used alternative for constructing shape functions in most of meshfree methods proposed so far. Two excellent features make it more popular than other interpolant scheme: (1) the approximated

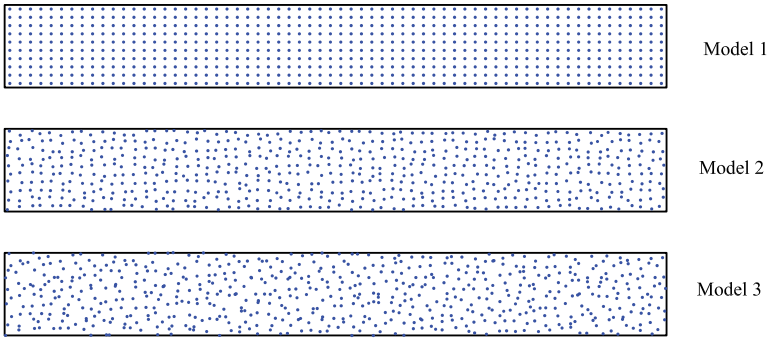

Figure 5: Three discretized models of the cantilever beam by different nodal irregularities

field is continuous and smooth over the entire problem domain; and (2) it is capable of producing an approximation in desired order of consistency and compatibility. Unfortunately, the *moment matrix* inversion is always required, and the inverse of this matrix does not exist sometimes when the number of nodes is small or the nodes scatter collinearly in some cases. By orthonormalizing basis functions, an improved MLS is formulated to overcome above inherent drawbacks.

3.1 Briefing the moving least-square

Consider a field $u(\mathbf{x})$ defined in the 2D domain Ω with boundary $\vec{A}$, which can be approximated over the poly-cell local support in the following form

$$u(\mathbf{x}) \approx u^h(\mathbf{x}) = \sum_{i=1}^{n} a_i(\mathbf{x}) p_i(\mathbf{x}) = \mathbf{a}^T(\mathbf{x})\mathbf{p}(\mathbf{x}) \tag{5}$$

where $\mathbf{p}(\mathbf{x})$ is a vector of basis functions built by the Pascal's triangles, $\mathbf{a}(\mathbf{x})^T=\{a_1(\mathbf{x}), a_2(\mathbf{x}),\ldots, a_m(\mathbf{x})\}$ is a vector of unknown parameters that depends on $\mathbf{x}^T=[x, y]$, and n is the number of nodes inside the local support. For two dimensions, basis function $\mathbf{p}$(x) of order 1 and 2 is written respectively by

$$\mathbf{p}^T(\mathbf{x}) = \begin{Bmatrix} p_1(\mathbf{x}) & p_2(\mathbf{x}) & p_3(\mathbf{x}) \end{Bmatrix} = \begin{Bmatrix} 1 & x & y \end{Bmatrix} \quad m = 3 \tag{6}$$

$$\mathbf{p}^T(\mathbf{x}) = \begin{Bmatrix} p_1(\mathbf{x}) & p_2(\mathbf{x}) & \cdots & p_6(\mathbf{x}) \end{Bmatrix} = \begin{Bmatrix} 1 & x & y & xy & x^2 & y^2 \end{Bmatrix} \quad m = 6 \tag{7}$$

where m is the number of monomial terms.

Note that the coefficient $a_i(\mathbf{x})$ is an arbitrary function of interested node $\mathbf{x}$, and m is usually much smaller than n. To determine $\mathbf{a}(\mathbf{x})$, a quadratic functional $I(\mathbf{x})$ is

constructed using the approximated values of field function $u^h(\mathbf{x})$ and the nodal parameters, u_i=$u(\mathbf{x}_i)$ as

$$I(\mathbf{x}) = \sum_{i=1}^{n} \left[w_i \left(\mathbf{a}^T(\mathbf{x})\mathbf{p}(\mathbf{x}) - u_i \right)^2 \right] \tag{8}$$

in which w_i is a weight function. The stationarity of Eq. (8) with respect to $\mathbf{a}$(x) leads to the following linear equation system:

$$\mathbf{a}(\mathbf{x}) = \mathbf{A}^{-1}(\mathbf{x})\mathbf{B}(\mathbf{x})\mathbf{u} \tag{9}$$

where the *moment matrix* $\mathbf{A}$ and basis matrix $\mathbf{B}$ are expressed respectively

$$\mathbf{A}(\mathbf{x}) = \sum_{i=1}^{n} w_i(\mathbf{x})\mathbf{p}(\mathbf{x}_i)\mathbf{p}^T(\mathbf{x}_i) \tag{10}$$

$$\mathbf{B}(x) = \begin{bmatrix} w_1(\mathbf{x})\mathbf{p}(\mathbf{x}_1) & w_2(\mathbf{x})\mathbf{p}(\mathbf{x}_2) & \cdots & w_n(\mathbf{x})\mathbf{p}(\mathbf{x}_n) \end{bmatrix} \tag{11}$$

$$\mathbf{u} = (u_1, u_2, \cdots, u_n)^T \tag{12}$$

Substituting Eq. (9) back into Eq. (5) leads to

$$u^h(x) = \sum_{i=1}^{n} \varphi_i u_i = \mathbf{\Phi}^T \mathbf{u} \tag{13}$$

and

$$\mathbf{\Phi}^T(\mathbf{x}) = \mathbf{p}^T(\mathbf{x})\mathbf{A}^{-1}(\mathbf{x})\mathbf{B}(\mathbf{x}) = \begin{Bmatrix} \varphi_1(\mathbf{x}) & \varphi_2(\mathbf{x}) & \ldots & \varphi_n(\mathbf{x}) \end{Bmatrix} \tag{14}$$

is the matrix of the usual MLS shape function.

The derivative of shape function Φ is given as

$$\mathbf{\Phi}^T_{,\mathbf{x}}(\mathbf{x}) = \mathbf{p}^T_{,\mathbf{x}} \cdot \mathbf{A}^{-1} \cdot \mathbf{B} + \mathbf{p}^T \cdot (\mathbf{A}^{-1})_{,\mathbf{x}} \cdot \mathbf{B} + \mathbf{p}^T \cdot \mathbf{A}^{-1} \cdot \mathbf{B}_{,\mathbf{x}} \tag{15}$$

where a comma designates a partial derivative with respect to the indicated spatial variable $\mathbf{x}$.

It can be clearly seen that the inversion of *moment matrix* $\mathbf{A}$ have to be performed frequently in both Eq. (14) and Eq. (15). Only the requirement of n»m is satisfied can prevent the singularity of the weighted moment matrix $\mathbf{A}$. Importantly, it is very probable that the inversion of $\mathbf{A}$ does not exist especially for the case of arbitrarily distributed nodes in the local circle support of interested node. On the other hand, the frequent operation of matrix inversion usually results in the computationally expensive cost. It is therefore, necessary to pursue some kind of special technique to avoid the frequent inversion operation of moment matrix $\mathbf{A}$ in the presence of higher order smoothness of the MLS shape functions.

3.2 Improved moving least-square

An improved MLS approximation is then formulated by orthonormalizing the basis functions **p** utilized in the conventional MLS [Lu, Belytschko and Gu (1994), Li and Liu (2002)]. This scheme not only can ensure the existence of inversion of coefficient matrix but extend our mind to connect different approximation scheme used in different kinds of meshfree methods.

Firstly, define a symbol operator as below

$$(f(\mathbf{x}),g(\mathbf{x}))_w = \sum_{i=1}^{n} f(\mathbf{x}_i)g(\mathbf{x}_i)w(\mathbf{x}_i) \tag{16}$$

where f and g can be arbitrary functions, n is the number of supporting nodes, $\mathbf{x}_i$denotes coordinates of the node i, and $w_i(\mathbf{x})$ is a weight vector same to MLS.

3.2.1 Orthogonalizing vector $\boldsymbol{p}$

The basis vector can be orthogonalized to avoid the frequent inversion of matrix by the standard Schmitt orthogonal process. However, in order to obtain a simpler form to program and implement, the basis functions are reorganized and the vector **p** can be orthogonalized firstly as follows

$$\mathbf{s} = \{s_1, s_2, ..., s_m\}^{\mathrm{T}} = \mathbf{V}\mathbf{p} \tag{17}$$

where **V** is an orthogonalizing matrix with dimension of $m \times m$. Assume V_{ij} is the elementary of **V** in line i and column j, and then V_{ij} can be computed by

$$V_{ij} = \begin{cases} 0 \text{ if } (i < j) \\ 1 \text{ if } (i = j) \\ -\sum_{k=j}^{i-1} \frac{(p_i,s_k)_w}{(s_k,s_k)_w} V_{kj} \text{if } (i > j) \end{cases} \qquad (i,j = 1,2,\ldots,m) \tag{18}$$

The proof of Eq. (18) by Schmidt orthogonalizing formulas is given as below.

Proof

The standard Schmidt orthogonal operation is as follows:

$$s_1 = p_1 \tag{19}$$

$$s_2 = p_2 - \frac{(p_2^{\cdot} s_1)_w}{(s_1,s_1)_w} \times s1 \tag{20}$$

...

$$s_i = p_i - \sum_{k=1}^{i-1} \frac{(p_i^{\cdot} s_k)_w}{(s_k,s_k)_w} \times s_k \tag{21}$$

Substituting Eq. (17) into Eq. (21) yields

$$\beta_i = p_i - \sum_{k=1}^{i-1} \sum_{j=1}^{m} \frac{(p_i, s_k)_w}{(s_k, s_k)_w} \times V_{kj} s_j \tag{22}$$

in which s_i is computed with $p_1, p_2, \ldots, p_i$. Note that when $j > k$, V_{kj}=0, hence

$$s_i = p_i - \sum_{k=1}^{i-1} \sum_{j=1}^{k} \frac{(p_i, s_k)_w}{(s_k, s_k)_w} \times V_{kj} p_j \tag{23}$$

$$= p_i - \sum_{j=1}^{i-1} \left(\sum_{k=j}^{i-1} \frac{(p_i, s_k)_w}{(s_k, s_k)_w} \times V_{kj} \right) p_j \tag{24}$$

Denote Eq. (24) in the matrix form and then Eq. (18) can be obtained.

3.2.2 *Normalizing vector* **s**

Normalizing the vector **s** yields

$$\mathbf{r}(\mathbf{x}) = \begin{Bmatrix} r_1(\mathbf{x}) & r_2(\mathbf{x}) & \ldots & r_m(\mathbf{x}) \end{Bmatrix}^{\mathrm{T}} \tag{25}$$

$$r_i = \frac{s_i}{\sqrt{(s_i, s_i)_w}} \; i = 1, 2, ..., m \tag{26}$$

Substituting Eq. (17) into Eq. (26) yields

$$\mathbf{r} = \mathbf{H}\mathbf{p} \tag{27}$$

where **H** is an orthonormalizing matrix with dimension of $m \times m$. Suppose H_{ij} is the elementary of **H** in line i and column j, and then H_{ij} can be computed by

$$H_{ij} = \frac{V_{ij}}{\sqrt{(s_i, s_i)_w}} \quad (i, j = 1, 2, ..., m) \tag{28}$$

3.2.3 *Computing shape functions* $\hat{\mathbf{O}}$

Now use the vector r as the basis vector and substitute **r** as **p** into Eq. (5) of standard MLS. A similar form of shape functions will be obtained as follows

$$\mathbf{\Phi}^T = \mathbf{r}^T(\mathbf{x})\mathbf{A}^{-1}\mathbf{B} \tag{29}$$

$$\mathbf{A}(\mathbf{x}) = \sum_{i=1}^{n} w_i(\mathbf{x})\mathbf{r}(\mathbf{x}_i)\mathbf{r}^T(\mathbf{x}_i) \tag{30}$$

$$\mathbf{B}(\mathbf{x}) = \begin{bmatrix} w_1(\mathbf{x})\mathbf{r}(\mathbf{x}_1) & w_2(\mathbf{x})\mathbf{r}(\mathbf{x}_2) & \cdots & w_n(\mathbf{x})\mathbf{r}(\mathbf{x}_n) \end{bmatrix} \tag{31}$$

Since the vector $\mathbf{r}$ is an orthonormalized vector, matrix $\mathbf{A}$ will be an identical matrix, and then the modified shape functions is

$$\mathbf{\Phi}^T = \mathbf{r}^T(\mathbf{x})\mathbf{B} \tag{32}$$

The partial derivative of shape function $\mathbf{\Phi}$ can be easily obtained as

$$\mathbf{\Phi}^T_{,\mathbf{x}} = \mathbf{r}^T_{,\mathbf{x}}\mathbf{B} + \mathbf{r}^T\mathbf{B}_{,\mathbf{x}} \tag{33}$$

It can be found that, the improved MLS is conducted without any inversion of matrix. This feature makes it more advantageous to very irregular node distribution for creating the shape functions. This also implies the MPG very robust in simulating problems of cracks and complex geometries. Furthermore, the improved MLS can work with any number of nodes in the poly-cell local support. When n>m, the improved MLS is referred to as the standard MLS; and when $n \leq m$, it can still be performed without any problems. This flexibility of selecting nodes indicates that fewer nodes can be used for the function interpolation and domain integration.

Fig.2(a) gives an example of nodal interpolation. Both the MLS and improved MLS are used for comparison and the weight functions are considered to be constant values. In standard MLS, linear base functions are adopted because the there are only four supporting nodes. However, in the improved MLS, quadratic base functions are adopted and four independent terms will be selected automatically. Fig.2(b) and Fig.2(c) shows the shape functions of a corner node. It can be observed that higher order of shape functions can be obtained for given number of nodes.

4 Discretized system equations

The Nitsche's method is used to treat the essential boundary conditions. The extended Galerkin weak form is derived for elasticity problems. Consider a 2D solid defined in Ω bounded by $\vec{A}$ ($\vec{A} = \vec{A}_t + \vec{A}_u$), the governing equations are given by

$$\nabla\sigma + \mathbf{b} = 0 \text{ in } \Omega \tag{34}$$

$$\sigma \cdot \mathbf{n} = \mathbf{t}_\Gamma \text{ on } \Gamma_t \tag{35}$$

$$\mathbf{u} = \mathbf{u}_\Gamma \text{ on } \Gamma_u \tag{36}$$

Using the Nitsche's method [Sonia and Antonio (2004)], the extended Galerkin

weak form for elasticity problems can be obtained as

$$\int_{\Omega}(\mathbf{L}\delta\mathbf{u})^T\mathbf{DLu}d\Omega-\int_{\Gamma_u}\delta\mathbf{u}^T\mathbf{t}d\Gamma-\int_{\Gamma_u}\delta\mathbf{t}^T\mathbf{u}d\Gamma+\beta\int_{\Gamma_u}\delta\mathbf{u}^T\mathbf{u}d\Gamma=$$
$$\int_{\Omega}\delta\mathbf{u}^T\mathbf{b}d\Omega+\int_{\Gamma_t}\delta\mathbf{u}^T\mathbf{t}_{\Gamma}d\Gamma-\int_{\Gamma_u}\delta\mathbf{t}^T\mathbf{u}_{\Gamma}d\Gamma+\beta\int_{\Gamma_u}\delta\mathbf{u}^T\mathbf{u}_{\Gamma}d\Gamma \quad (37)$$

where $\mathbf{L}$ is the differential operator, and β is a positive constant scalar that ensures the coercivity of the bilinear form. The value of β sharply influences the accuracy of numerical solutions, which is thoroughly examined in the following patch test.

To obtain the discretized system, the approximation $\mathbf{u}$ in Eq. (5) is substituted into the weak form of Eq. (37), which leads to the following matrix form

$$\mathbf{Kq}=\mathbf{f} \quad (38)$$

where

$$\mathbf{K}_{IJ}=\int_{\Omega}\mathbf{B}_I^T\mathbf{DB}_J d\Omega-\int_{\Gamma_u}\Phi_I^T\mathbf{SNDB}_J d\Gamma-\int_{\Gamma_u}\mathbf{B}_I^T\mathbf{D}^T\mathbf{N}^T\mathbf{S}\Phi_J d\Gamma+\beta\int_{\Gamma_u}\Phi_I^T\Phi_J d\Gamma \quad (39)$$

$$\mathbf{f}_I=\int_{\Gamma_t}\Phi_I^T\mathbf{t}_{\Gamma}d\Gamma+\int_{\Omega}\Phi_I^T\mathbf{b}d\Omega+\int_{\Gamma_u}\mathbf{B}_I^T\mathbf{D}^T\mathbf{N}^T\mathbf{Su}_{\Gamma}d\Gamma+\beta\int_{\Gamma_u}\Phi_I^T\mathbf{u}_{\Gamma}d\Gamma \quad (40)$$

$$\mathbf{B}_I=\begin{bmatrix}\frac{\partial\Phi_I}{\partial x} & 0 & \frac{\partial\Phi_I}{\partial y}\\ 0 & \frac{\partial\Phi_I}{\partial y} & \frac{\partial\Phi_I}{\partial x}\end{bmatrix}^T \quad (41)$$

$$\mathbf{N}=\begin{bmatrix}n_x & 0 & n_y\\ 0 & n_y & n_x\end{bmatrix} \quad (42)$$

and

$$\mathbf{S}=\begin{bmatrix}s_x & 0\\ 0 & s_y\end{bmatrix} \quad (43)$$

$$s_x=\begin{cases}1, \text{ if prescribed } u_x \text{ on } \Gamma_u\\ 0, \text{ if not prescribed } u_x \text{ on } \Gamma_u\end{cases} \qquad s_y=\begin{cases}0, \text{ if prescribed } u_y \text{ on } \Gamma_u\\ 1, \text{ if not prescribed } u_y \text{ on } \Gamma_u\end{cases} \quad (44)$$

For elastic plane stress problems the material matrix $\mathbf{D}$ is represented by Young's modulus E and Poisson's ratio ν as

$$\mathbf{D}=\frac{E}{1-\nu^2}\begin{bmatrix}1 & \nu & 0\\ \nu & 1 & 0\\ 0 & 0 & \frac{1-\nu}{2}\end{bmatrix} \quad (45)$$

For plane strain problems, Eq. (45) holds by substituting E and ν with $E/(1-\nu^2)$ and $\nu/(1-\nu)$, respectively.

5 Numerical examples

An intensive numerical study for the proposed MPG is conducted using a number of elasticity and fracture problems. The variable units used in this paper are based on international standard unit system unless specially denoted.

To study the convergence property of the MPG, two error indicators in displacement and energy are, respectively, defined as follows:

$$||\mathbf{u}-\mathbf{u}^{exact}||_2 = \sqrt{\int_\Omega (\mathbf{u}^{exact}-\mathbf{u}^{numerical})^2 d\Omega} \tag{46}$$

$$\left\|\mathbf{u}-\mathbf{u}^{exact}\right\|_e = \sqrt{\frac{1}{2}\int_\Omega (\boldsymbol{\varepsilon}^{exact}-\boldsymbol{\varepsilon}^{numerical})^T \mathbf{D} (\boldsymbol{\varepsilon}^{exact}-\boldsymbol{\varepsilon}^{numerical}) d\Omega} \tag{47}$$

where the superscript *exact* notes the exact or analytical solution, *numerical* denotes a numerical solution obtained using a numerical method including the MPG.

The parameter α in weight functions will be studied in the cantilever beam problem and in other examples of this paper, α is evaluated 4.0 in this work. For all the examples of this paper, linear basis is used for the improved MLS scheme. The penalty factor β in Nitche's method is evaluated $100\times E$. For each cell of background mesh, 3×3 Gaussian quadrature is used except the cells crossed by cracks, where 5×5 Gaussian quadrature is used. The cells crossed the geometrical boundaries will be divided into 2×2 subcells to reduce the error of integration.

5.1 Standard patch test

For a numerical method working well for solid mechanics problems, the sufficient requirement for convergence is to pass the standard patch test [Zienkiewicz and Taylor (2000)]. Therefore, the first example is the standard patch test evaluated by the present MPG. The problem is studied in a domain of dimension 1×1, and the displacements are prescribed on all outside boundaries by the following linear function.

$$u_x = x \tag{48}$$

$$u_y = y \tag{49}$$

In the MPG, 2×2 background mesh is adopted and the patch is represented by two models (4 regular nodes and 4 irregular nodes) as shown in Fig. 3. The errors in displacement for different β of the three models are listed in Table 1.

Table 1: Relative error ($||u-u^{exact}||_2/||u^{exact}||_2$) for different β in the patch test

β	Grid a	Grad b
10000×E	6.387494157597449E-012	5.448332276743418E-009
100000×E	6.385993036423848E-013	5.448282241520079E-010
1000000×E	6.385960373324049E-014	5.448291486880150E-011
10000000×E	6.417295611370838E-015	5.448495876062633E-012
100000000×E	8.659913793448943E-016	5.450119488224402E-013

The computational results show that, with the increasing of penalty parameter β, the accuracy of numerical solutions is improved significantly. Thus it is suggested that there exists an optimal numerically conformed number of β such that the MPG solution is closest to the exact result. Too large β produces an ill-conditioned stiffness matrix, and hence results in a low efficiency for solving the complicated problems.

It is observed that the β value varied from $10^4 \sim 10^8 \times E$ can provide acceptable accuracy, which is preferred in the following numerical examples. Though nodal irregularity distribution decreases the accuracy of numerical solutions in the patch test, the MPG solution is more closest to exact solution compared with those obtained using EFG and NEM [Sukumar, Moran and Belytschko (1998)].

In conclusion, numerical results indicate the present MPG passes the patch test and monotonically converges due to its capable of reproducing linear fields.

5.2 Cantilever beam

A 2D cantilever beam with length L, height D and unit thickness is studied as a benchmark problem here. The beam is fixed at the left end and subjected to a parabolic traction P at the free end as shown in Fig. 4. The analytical solutions in displacement and stress are available [Timoshenko and Goodier (1970)] as follows

$$u_x = -\frac{P(y-D/2)}{6EI}\left[(6L-3x)x+(2+\nu)(y^2-2Dy)\right] \tag{50}$$

$$u_y = \frac{P}{6EI}\left[3\nu(y-\frac{1}{2}D)^2(L-x)+\frac{1}{4}(4+5\nu)D^2x+(3L-x)x^2\right] \tag{51}$$

$$\sigma_{xx} = -\frac{P}{I}(L-x)\left(y-\frac{1}{2}D\right) \tag{52}$$

$$\sigma_{yy} = 0 \tag{53}$$

$$\sigma_{xy} = -\frac{Py}{2I}(y-D) \tag{54}$$

where I is the moment of the inertia given as $I=D^3/12$.

The problem is solved for the plane stress case, in which the parameters are taken as: L=8, D=1, P=-1, $E=3.0\times10^7$ and ν=0.25.

5.2.1 *Effects of nodal irregularity*

To investigate the influence of nodal irregularities on the accuracy and convergence of numerical solutions, a 10×64 background mesh is adopted and three models with different degree of nodal irregularity (shown in Fig. 5) are used to examine the present approach. The results of computed deflection along the neutral line are plotted in Fig. 6a, together with the analytical solutions. Fig. 6b shows the stress in x direction along the line ($x = L/2$) of the beam, the analytical solution is also given.

It can be found that the numerical results of these three models obtained using the present MPG are all in very good agreement with the analytical ones, and the irregularity of the nodal distribution has little effect on the numerical results.

5.2.2 *Convergence study*

In the convergence study, three regular background meshes are used (4×10, 6×15 and 8×20) and in each cell a centered node is distributed. To study the effect of parameter α, the convergence curves for α=3 and α=4 are plotted in displacement and energy norm, respectively in Fig. 7a and b, in which the convergence rates (generally the ratio of error norm to characteristic nodal spacing) are indicated by R.

It can be clearly observed that MPG can provide the superconvergent solution and the convergence rates for both αÂ£Â½3 and αÂ£Â½4 significantly exceed the counterparts of FEM, in which the theoretical value is 2.0 for displacement and 1.0 for energy. In addition, compared with FEM, MPG also achieves more accurate solutions, especially when α is increased. Thus, α is selected to be 4.0 as the optimal parameter.

5.3 *An infinite plate with a hole*

Fig. 8 is the infinite plate with a central hole subjected to a tensile traction P of 1. Due to its symmetric, only the upper right quadrant of the plate is modeled with the dimensions of b in both x and y directions. The analytical stress can be found in [Atluri, Liu and Han (2006), Roark and Young (1975)] in the polar coordinate form:

$$\sigma_{xx} = P\left\{1-\frac{a^2}{r^2}\left[\frac{3}{2}\cos 2\theta+\cos 4\theta\right]+\frac{3a^4}{2r^4}\cos 4\theta\right\} \tag{55}$$

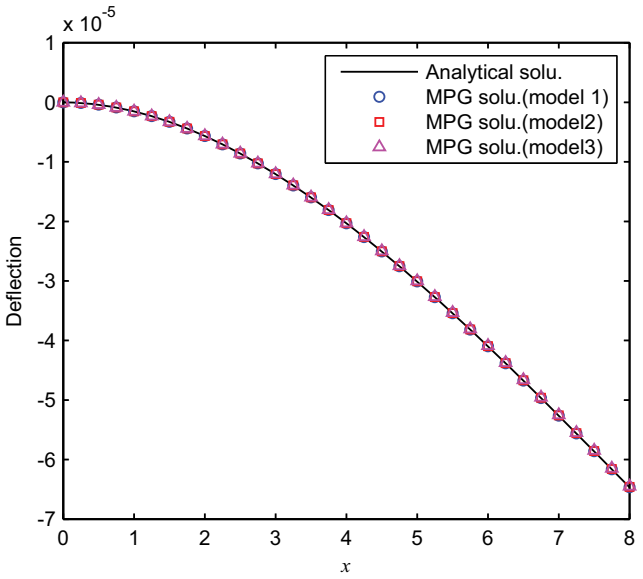

(a) Deflection distribution along the neutral line of the Cantilever beam.

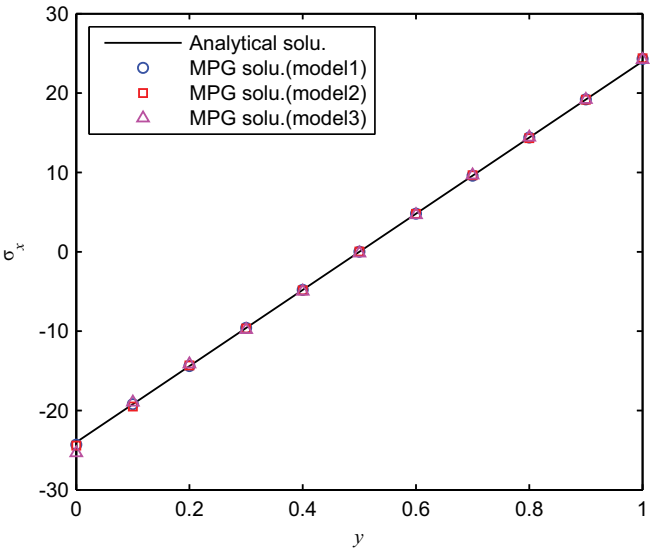

(b) Stress distribution in the x direction along the line ($x = L/2$).

Figure 6: Comparisons of numerical results obtained from MPG and the exact solution

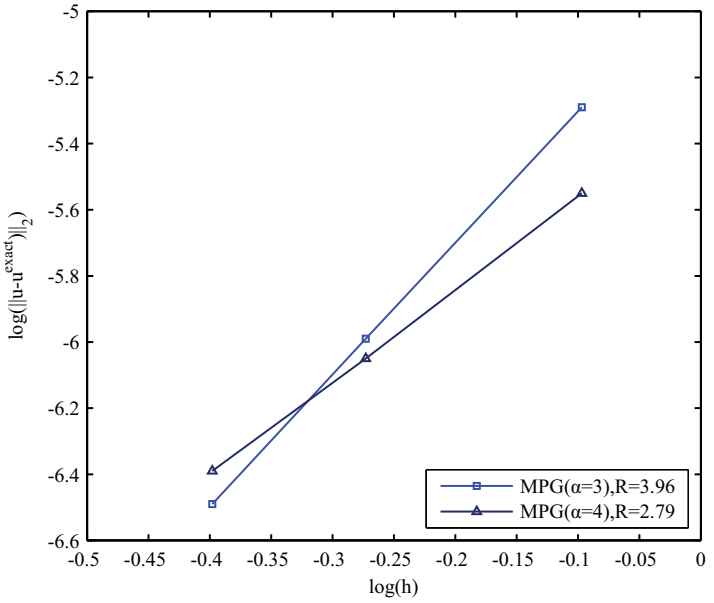

(a) Displacement error norm.

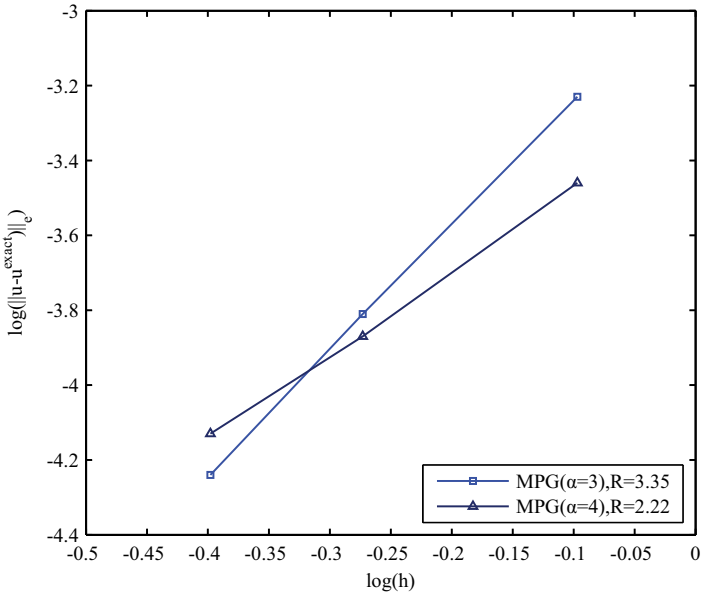

(b) Energy error norm.

Figure 7: Convergence comparisons for different α in displacement and energy norm

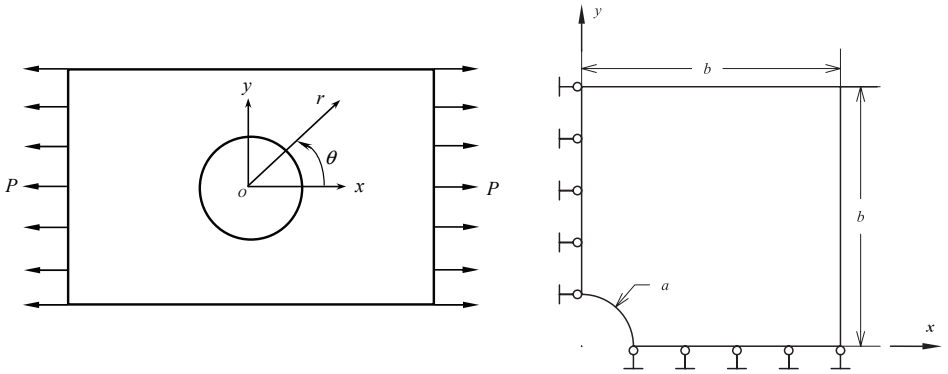

Figure 8: Infinite plate with a circular hole subjected to unidirectional tension and its quarter model (a=0.2, b=1)

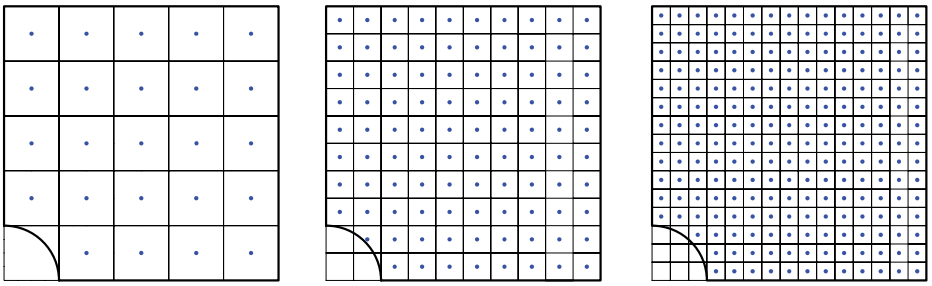

Figure 9: Three discretized models of the quarter infinite plate with a circular hole

$$\sigma_{yy} = -P\left\{\frac{a^2}{r^2}\left[\frac{1}{2}\cos 2\theta - \cos 4\theta\right] - \frac{3a^4}{2r^4}\cos 4\theta\right\} \tag{56}$$

$$\sigma_{xy} = -P\left\{\frac{a^2}{r^2}\left[\frac{1}{2}\sin 2\theta + \sin 4\theta\right] + \frac{3a^4}{2r^4}\sin 4\theta\right\} \tag{57}$$

where θ is measured counterclockwise from the positive x-axis. Traction boundary conditions are enforced at x=1.0 and y=1.0 based on the above analytical solutions. Similarly, the analytical displacement of the plate is given as

$$u_r = \frac{P}{4\mu}\left\{r\left[\frac{\kappa-1}{2} + \cos 2\theta\right] + \frac{a^2}{r}[1 + (1+\kappa)\cos 2\theta] - \frac{a^4}{r^3}\cos 2\theta\right\} \tag{58}$$

$$u_\theta = \frac{P}{4\mu}\left[(1-\kappa)\frac{a^2}{r} - r - \frac{a^4}{r^3}\right]\sin 2\theta \tag{59}$$

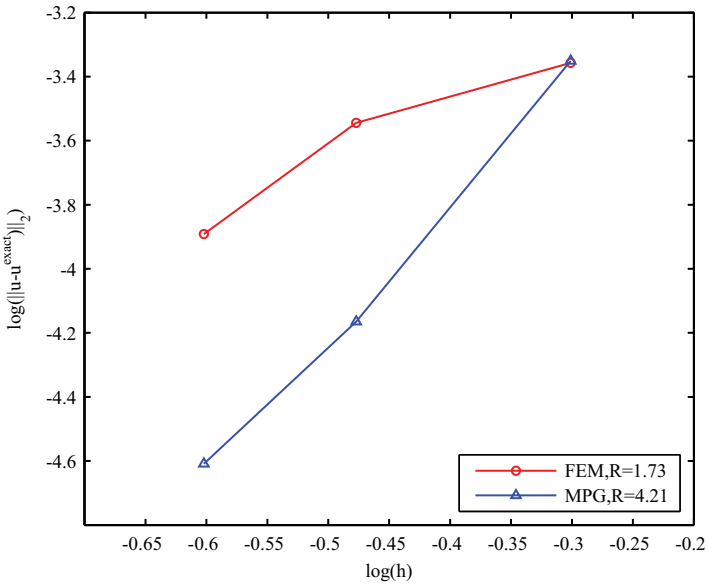

(a) Displacement in L_2 norm.

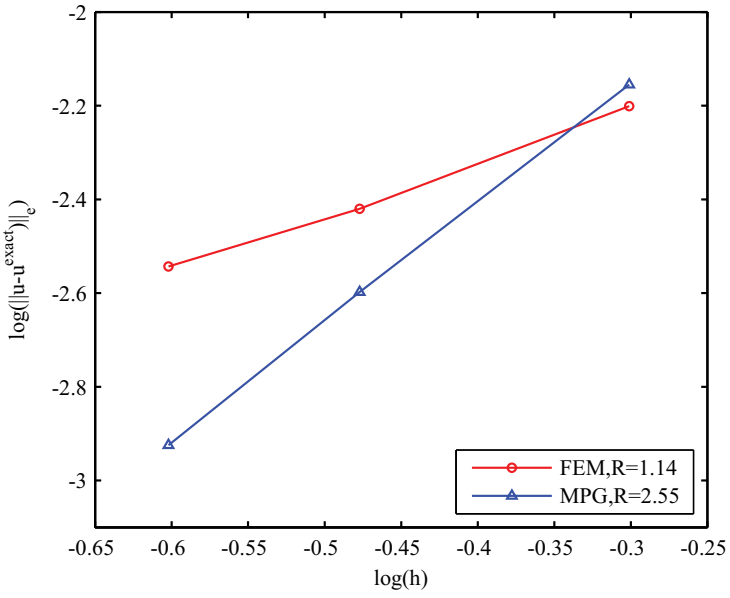

(b) Energy norm.

Figure 10: Comparisons of convergence rates between the present MPG and FEM

where

$$\mu = \frac{E}{2(1+\mu)},\ \kappa = \begin{cases} 3-4\upsilon \text{ Plane strain} \\ \frac{3-\mu}{1+\mu} \text{ Plane stress} \end{cases} \tag{60}$$

The essential boundary conditions are $u(x{=}0){=}0$, $v(y{=}0){=}0$. The material used is linear elastic with Young's modules $E{=}1.0{\times}10^3$ and poison's ratio $\nu{=}0.3$. The other parameters in this problem are taken as: $a{=}1$ and $b{=}5$. The beam has a unit thickness, and is taken as a plane strain problem.

Three types of regular background meshes are used ($5{\times}5$, $10{\times}10$ and $15{\times}15$) and the $5{\times}5$ mesh is shown in Fig.9 The convergence rates in both displacement norm and energy norm are plotted in Fig. 10a and b, respectively.

It can be observed that the MPG achieves better accuracy and higher convergence rates of 4.21 and 2.55 in displacement and energy norm, respectively. These numerical rates are much larger than theoretical values and FEM, which show that the MPG presents the superconvergent property.

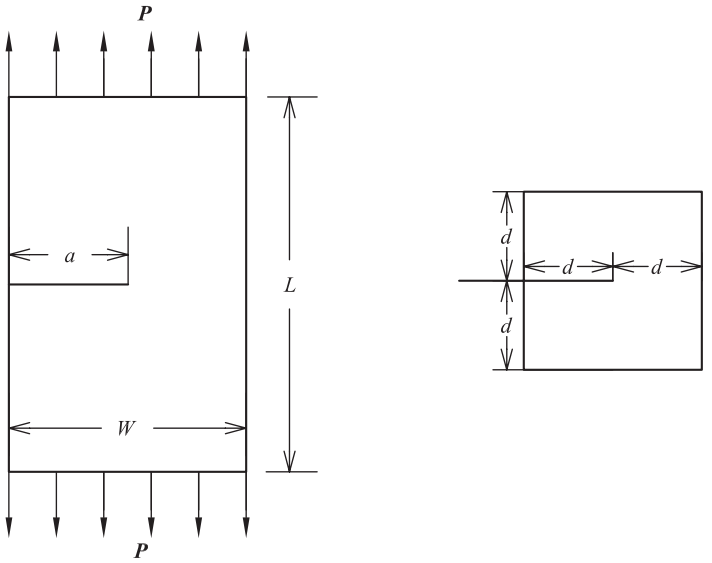

Figure 11: Single edge-cracked plate under mode-I loading

5.4 Edge crack

A rectangular plate with an edge crack of length a is shown in Fig. 11a. The values of the parameters are taken as: $W{=}1$, $L{=}2$, $P{=}1$.

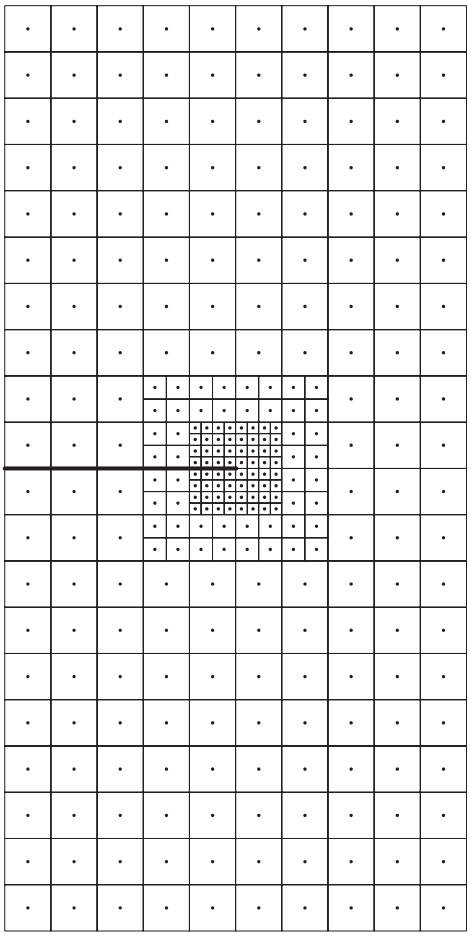

Figure 12: Meshfree background mesh for the edge crack problem

The stress intensity factors are evaluated by using the conservation integral which is converted into the domain integral by using Green's theorem [Chow and Atluri (1998), Budiansky and Rice (1973), Li and Shih (1985)]. The domain of conservation integral is represented in Fig. 11b.

For comparison, two initial background meshes of 10×20 and 20×40 are used and the initial meshes are refined hierarchically in the crack tip. Fig. 12 plots the 10×20 mesh after 2 times of local refinement. Fig. 13a shows errors of stress intensity factors (K_1) with respect to different refinement times n when crack length

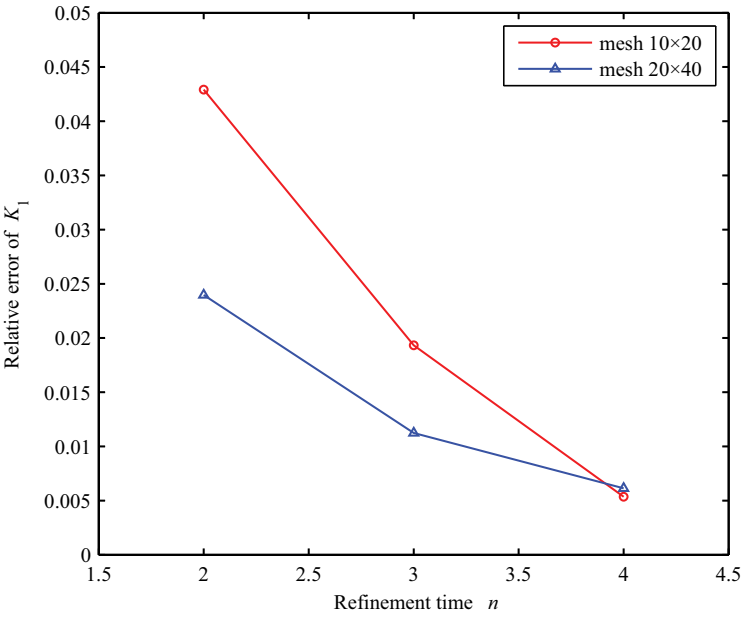

(a) Error for different times of local refinement.

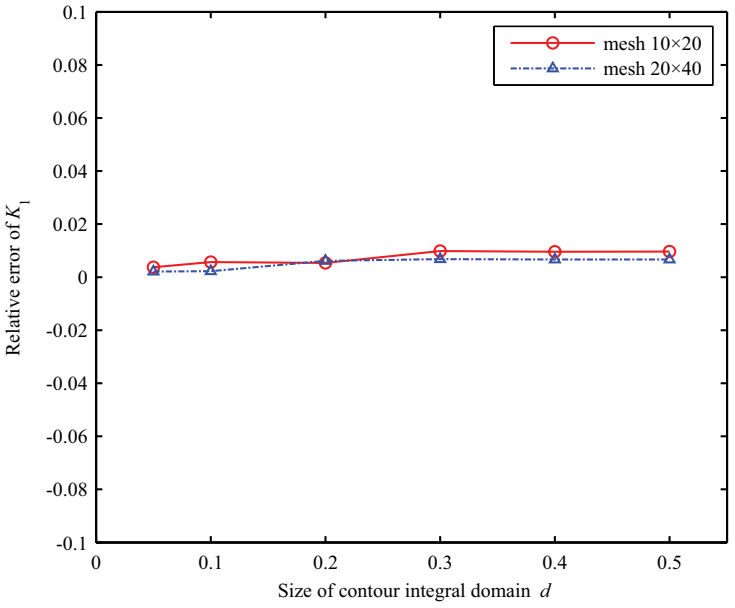

(b) Error for different contour integral domain.

Figure 13: Error comparisons of the K_1

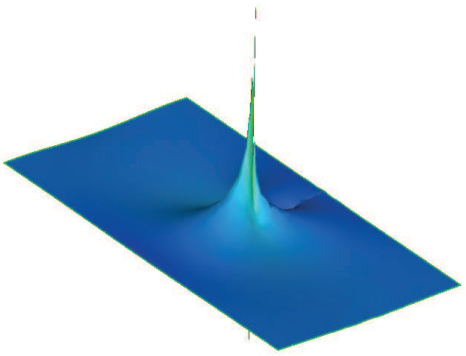

(a) Stress contour of σ_x.

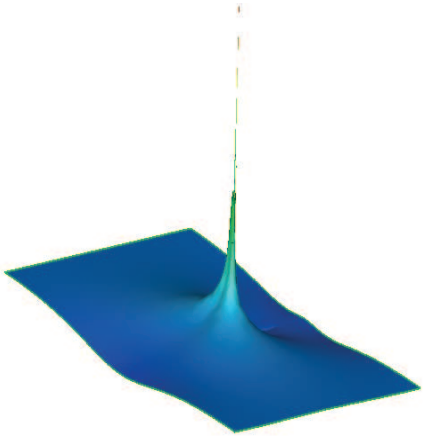

(b) Stress contour of σ_y.

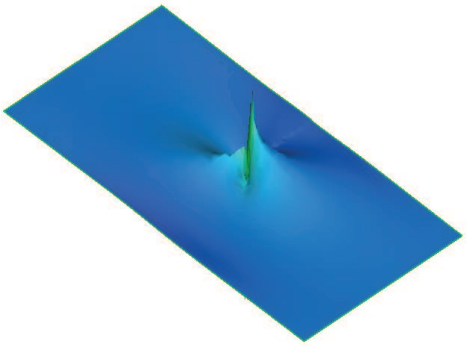

(c) Stress contour of τ_{xy}.

Figure 14: Contour of stress field of the edge crack problem

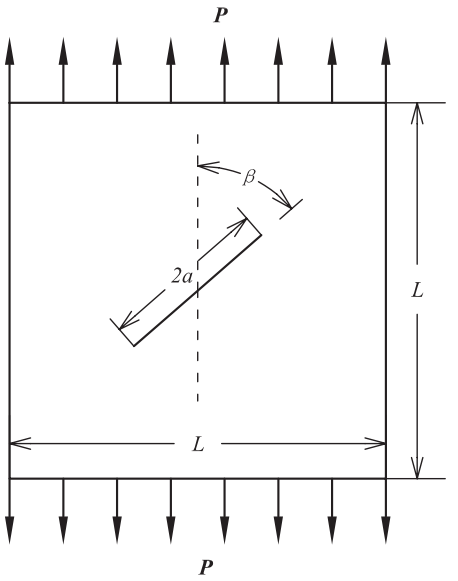

Figure 15: Center-oblique crack plate under uniaxial loading

is a=0.5.

It can be clearly seen that the refinement can improve the accuracy significantly, and 4 times of local refinement can provide the best accuracy using the mesh of 10×20, compared with the mesh of 20×40. This also indicates that we only need to refine around the crack tip.

When crack length is 0.5 and refinement time is 4, the normalized K_1 with different domain size d of conservation integral is plotted in Fig. 13b.

It is well-known that the integration path generally influences the accuracy of numerical solutions for both FEM and meshfree methods with circular local support [Belytschko, Lu and Gu (1995)]. In the MPG, poly-cell local support is used to tackle this problem. It can be found from Fig. 13b that, the stress intensity factor evaluated using the present MPG is completely path-independent.

Since the coarse mesh can provide the satisfying results, background mesh of 10×20 is then used to compute the stress intensity factor K_1. Table 2 shows the normalized K_1 of different crack length when 10×20 initial mesh is used and refinement time is 4. It can be observed that K_1 evaluated by MPG is closed to the analytical value.

For examination of gradient field especially for the crack tip field, the stress dis-

Table 2: Normalized K_1 for edge crack with different crack length

a	0.2	0.21	0.22	0.23	0.24	0.25	0.3	0.4	0.5
Numerical K_1	1.0917	1.1359	1.1909	1.2373	1.2870	1.3392	1.6156	2.3808	3.5640
Analytical K_1	1.0865	1.1328	1.1803	1.2289	1.2789	1.3302	1.6115	2.3580	3.5423
Normalized K_1	1.0048	1.0027	1.0090	1.0068	1.0063	1.0067	1.0025	1.0097	1.0061

tributions of σ_x, σ_y, and τ_{xy} are also plotted in Fig. 14a, b, and c, respectively, in which crack length is 0.5 and the 20×40 initial mesh is refined for 3 times.

It can be clearly seen that the stress field is special smoothing even near to the crack tip without any postprocessing operations. This excellent feature makes MPG very flexible and promising for crack analysis or the high gradient region.

5.5 Oblique crack

To further examine the numerical accuracy of the MPG in mixed-mode crack problems, an infinite plate with an inner oblique crack [Yau, Wang and Corten (1980)] is studied as shown in Fig. 15. The parameters are taken as: L=10, P=1, a=1.

The analytical stress intensity factors of this problem can be computed by

$$K_{\mathrm{I}} = \sigma \sin^2 \beta \sqrt{\pi a} \tag{61}$$

$$K_{\mathrm{II}} = \sigma \cos \beta \sin \beta \sqrt{\pi a} \tag{62}$$

Table 3: Normalized K_1 and K_2 for oblique crack problem with different crack angles

β	60°	55°	50°	45°	40°	35°	30°
Numerical K_1	0.9447	0.8490	0.7400	0.6290	0.5150	0.4160	0.3120
Analytical K_1	0.9400	0.8410	0.7354	0.6267	0.5179	0.4123	0.3133
Normalized K_1	1.0050	1.0099	1.0057	1.0036	0.9935	1.0099	0.9953
Numerical K_2	0.5487	0.5970	0.6200	0.6230	0.6180	0.5950	0.5470
Analytical K_2	0.5427	0.5889	0.6171	0.6267	0.6171	0.5889	0.5427
Normalized K_2	1.0110	1.0144	1.0055	0.9946	1.0021	1.0106	1.0106

A 20×20 initial mesh is used to refine for 4 times for two crack tips. Table 3 lists the normalized K_1 and K_2 of different oblique angle β, together with the analytical ones. It can be observed that both K_1 and K_2 are very close to the analytical values.

6 Conclusions

A new meshfree approach of the proposed MPG is formulated for elasticity and fracture problems. In the approach, the poly-cell local support replaces the usual circle support widely used in EFG and MLPG. The trial function is constructed using the improved MLS by orthonormalized the basis functions to guarantee working well for general nodal distribution. The Nitsche's method is introduced to enforce the essential boundary conditions weakly. Some examples are studied in details in terms of accuracy and superconvergence for the performance of the present MPG. From these examples, the following conclusions can be made as below:

(1) In elasticity problems, it is found that MPG can obtain more accurate solutions compared with FEM using the same nodal distributions. This improvement of numerical accuracy is mainly due to introducing the poly-cell local support.

(2) The convergence rates for MPG in displacement and energy norms are higher than those of theoretical values, which present the superconvergent property.

(3) In fracture problems, it is found that the stress intense factors obtained from the MPG are also more accurate. The relative errors are less than 1%.

(4) When the stress intense factor is evaluated by conservation integral, the present approach does not have the path-dependent problems.

(5) Gradient fields such the stress fields (σ_x, σ_y, and τ_{xy}) obtained using the present MPG are great smoothing even around the crack tip.

(6) MPG works very well for extremely distorted distribution in nodes mainly thanks to the use of the improved MLS approach and the poly-cell local support.

Acknowledgement: The authors give sincerely thanks to the support of Centre for ACES, National University of Singapore, Singapore-MIT Alliance (SMA). Special thanks are also given to Prof. Liu Gui-Rong for his constructive comments and suggestions.

References

Atluri, S.N.; Zhu, T.L. (1998): A new meshless local Petrov–Galerkin (MLPG) approach in computational mechanics, *Comput. Mech*, vol. 22, pp. 117–27.

Atluri, S.N.; Sladek, J.; Sladek, V.; Zhu, T. (2000): The local boundary integral equation (LBIE) and its meshless implementation for linear elasticity, *Computational Mechanics*, vol. 25, pp. 180-198.

Atluri, S.N., Shen, S.P. (2002): The meshless local Petrov-Galerkin (MLPG) method: A simple & lesscostly alternative to the finite element and boundary element methods, *CMES: Computer Modeling in Engineering and Sciences*, 3 (1) 11-51.

Atluri, S.N. (2004): The Meshless Local Petrov-Galerkin (MLPG) Method for Domain & Boundary Discretizations, *Tech Science Press*.

Atluri, S.N.; Han, Z.D.; Rajendran, A.M. (2004): A New Implementation of the Meshless Finite Volume Method, Through the MLPG "Mixed" Approach, *CMES: Computer Modeling in Engineering & Sciences*, vol. 6, no. 6, pp. 491-514.

Atluri, S.N.; Shen, S. (2005): The Meshless Local Petrov-Galerkin (MLPG) method, *Tech Science Press*, Encino, USA.

Atluri, S.N.; Liu, H.T.; Han, Z.D. (2006): Meshless local Petrov-Galerkin (MLPG) mixed collocation method for elasticity problems, *CMES: Computer Modeling in Engineering & Sciences*, 14 (3), 141-152.

Atluri, S.N.; Liu, H.T; Han, Z.D. (2006): Meshless local Petro-Galerkin (MLPG) mixed finite difference method for solid mechanics, *CMES: Computer Modeling in Engineering & Sciences*, vol. 15, pp. 1-16.

Budiansky, D.; Rice, J.R. (1973): Conservation laws and energy-release rates, *J. Appl. Mech*, vol. 40, pp. 201-203.

Belytschko, T.; Lu, Y.Y.; Gu, L. (1995): Crack propagation by element-free Galerkin methods, *Eng. Fract Mech*, vol. 51, pp. 295-315.

Belytschko, T.; Lu, Y.Y.; Gu, L. (1994): Element free Garlerkin methods, *Int. J. Numer. Meth. Engng*, vol. 37, pp. 229-256.

Beissel, S.; Belytschko, T. (1994): Nodal integration of the element-free Galerkin method, *Comput. methods Appl. Mech. Engrg*, vol. 139, pp. 49-74.

Brighenti, R. (2005): Application of the element-free Galerkin meshless method to 3D fracture mechanics problems, *Eng. Fract Mech*, vol. 72, pp. 2808-2820.

Braum, J.; Sambridge, M. (1995): A numerical method for solving partial differential equations on highly irregular evolving grids, *Nature*, vol. 375, pp. 665-660.

Ching, H.K.; Batra, R.C. (2001): Determination of crack tip fields in linear elastostatics by the meshless local Petrov-Galerkin (MLPG) method, *CMES: Computer Modeling in Engineering & Sciences*, vol. 12, pp. 273-289.

Chow, W.T.; Atluri, S.N. (1998): Stress intensity factors as the fracture parameters

for determination crack growth in composite laminates, *Comput. Mech*, vol. 21, pp. 1-10.

Cui, X.Y.; Liu, G.Y.; Li, G.Y.; Zhao, X.; Nguyen, T. T.; Sun, G.Y. (2008): A smoothed finite element method (SFEM) for linear and geometrically nonlinear analysis of plates and shells, *CMES: Computer Modeling in Engineering & Sciences*, vol. 28, pp. 109-125.

Fleming, M.; Chu, Y.A.; Moran, B.; Belytschko, T. (1997): Enriched element-free Galerkin methods for crack-tip fields, *Int. J. Numer. Meth. Engng*, vol. 40, pp. 1483-1504.

Fries, T.P.; Belytschko, T. (2008): Convergence and stabilization of stress-point integration in mesh-free and particle methods, *Int. J. Numer. Meth. Engng*, vol. 74, pp. 1067-1087.

Gu, Y.T.; Zhang, L.C. (2008): Coupling of the meshfree and finite element methods for determination of the crack tip fields, *Eng. Fract Mech*, vol. 75, pp. 986-1004.

Han, Z.D.; Atluri, S.N. (2004): Meshless Local Petrov-Galerkin (MLPG) approaches for solving 3D Problems in elasto-statics, *CMES: Computer Modeling in Engineering & Sciences*, vol. 6 no. 2, pp. 169-188.

Han, Z.D.; Rajendran, A.M; Atluri, S.N. (2005): Meshless Local Petrov-Galerkin (MLPG) Approaches for Solving Nonlinear Problems with Large Deformation and Rotation, *CMES: Computer Modeling in Engineering & Sciences*, vol. 10, no. 1, pp. 12.

Han, Z.D., Liu, H.T., Rajendran, A.M., et al. (2006): The applications of meshless local Petrov-Galerkin (MLPG) approaches in high-speed impact, penetration and perforation problems, *CMES: Computer Modeling in Engineering & Sciences*, vol. 14, no. 2, pp. 119-128.

Idelsohn, S.R.; Oñate, E.; Calvo, N.; Facundo, D.P. (2003): The meshless finite element method. *Int. J. Numer. Meth. Engng*, vol. 58, pp. 893-912.

Idelsohn, S.R.; Oñate, E. (2006): To mesh or not to mesh. That is the question. *Comput. methods Appl. Mech. Engrg*, vol. 195, pp. 4681-4696.

Lancaser, P.; Salkauskas, K. (1981): Surface generated by moving least squares methods. *Math. Comp*, vol. 37, pp. 141-158.

Li, S.F.; Liu, W.K. (2002): Meshfree and particle methods and their applications. *Appl. Mech. Rev*, vol. 55, pp. 1-34.

Li, F.Z.; Shih, F.C.A. (1985): Needleman. A comparison of methods for calculating energy release rates. *Eng. Fract Mech,* vol. 21, pp. 405-421.

Liu, G.R. (2002): *Meshfree methods: Moving Beyond the Finite Element Method*,

CRC Press, Boca Raton, USA.

Liu, W.K.; Jun, S.; Zhang, Y.F. (1995): Reproducing kernel particle methods, *Int. J. Numer. Meth. Fluids,* vol. 20, pp. 1081-1106.

Liu, G.R.; Zhang, G.Y.; Wang, Y.Y.; Zhong, Z.H.; Li, G.Y.; Han, X. (2006): A nodal integration technique for meshfree radial point interpolation method (NI-RPIM). *Int. J. Solids Struct*, vol. 44, pp. 3840-3860.

Lu, Y.Y.; Belytschko, T.; Gu, L. (1994): A new implementation of the Element-free Galerkin methods. *Comput. methods Appl. Mech. Engrg*, vol. 113, pp. 397-414.

Sladek, J. ; Sladek, V.; Atluri, S.N. (2004): Meshless local Petrov-Galerkin method in anisotropic elasticity, *CMES: Computer Modeling in Engn. & Sciences*, vol. 6, pp. 477-489.

Sladek, J.; Sladek, V.; Krivacek, J.; Zhang Ch. (2005): Meshless Local Petrov-Galerkin Method for stress and crack analysis in 3-D axisymmteric FGM bodies, *CMES: Computer Modeling in Engineering & Sciences*, vol. 8, pp. 259-270.

Sonia, F.M.; Antonio, H. (2004): Imposing essential boundary conditions. *Comput. methods Appl. Mech. Engrg,* vol. 193, pp. 1257-1275.

Sukumar, N,; Moran, B.; Belytschko, T. (1998): The natural element method in solid mechanics. *Int. J. Numer. Meth. Engng,* vol. 43, pp. 839-887.

Timoshenko, S.P.; Goodier, J.N. (1970): *Theory of Elasticity, third edition,* McGraw, New York, USA.

Roark, R.J.; Young, W.C. (1975): *Formulas for stress and strain*, McGraw, New York, USA.

Wu, S.C.; Liu, G.R.; Zhang, H.O.; Zhang G.Y. (2008): A node-based smoothed point interpolation method (NS-PIM) for three-dimensional thermoelastic problems, Numerical Heat Transfer: Part A: Applications, vol. 54, pp. 1121-1147.

Yau, J.; Wang, S.; Corten, H. (1980): A mixed-mode crack analysis of isotropic solids using conservation laws of elasticity. *J. Appl. Mech,* vol. 47, pp. 335-341.

Zheng, C.; Zhang, J.H.; Wu, S.C. (2008): A novel mesh-free poly-cell Galerkin (MPG) Method, *Acta Mechanic Sinica*, (in press).

Zienkiewicz, O.C.; Taylor, R.L. (2000): *The Finite Element Method, fifth edition*, Butterworth Heinemann, Oxford, UK.

Zhou, J.X.; Wen, J.B.; Zhang, H.Y.; Zhang, L. (2003): A nodal integration and post-processing technique based on Voronoi diagram for Galerkin meshless methods. *Comput. methods Appl. Mech. Engrg*, vol. 192, pp.3831–3843.